Inclusion-localised crystal-plasticity, dynamic porosity, and fast-diffusion pathway generation in zircon

Nicholas E. Timms [a,*], Steven M. Reddy [a], John D. Fitz Gerald [b], Leonard Green [c], Janet R. Muhling [d]

[a] Department of Applied Geology, Curtin University, GPO Box U1987, Perth, WA 6845, Australia
[b] Research School of Earth Sciences, Australian National University, Canberra 0200, Australia
[c] Adelaide Microscopy, University of Adelaide, Adelaide, SA 5005, Australia
[d] Centre for Microscopy, Characterisation and Analysis, University of Western Australia, Perth, WA 6009, Australia

ABSTRACT

A population of oscillatory zoned, igneous zircon grains in a Javanese andesite contains fluid and mineral inclusions (up to 10 μm across) trapped during zircon growth. Orientation contrast imaging and orientation mapping by electron backscatter diffraction reveal that crystal-plastic deformation overprints growth zoning and has localized around 1–10 μm pores and inclusions. Cumulative crystallographic misorientation of up to 25° around pores and inclusions in zircon is predominantly accommodated by low-angle (<5°) orientation boundaries, with few free dislocations in subgrain interiors. Low-angle boundaries are curved, with multiple orientation segments at the sub-micrometer scale. Misorientation axes associated with the most common boundaries align with the zircon c-axis and are consistent with dislocation creep dominated by <100>(010) slip. A distinctly different population of sub-micron pores is present along subgrain boundaries and their triple junctions. These are interpreted to have formed as a geometric consequence of dislocation interaction during crystal-plasticity. Dislocation creep microstructures are spatially related to differences in cathodoluminescence spectra that indicate variations in the abundance of CL-active rare earth elements. The extent of the modification suggests deformation-related fast-pathway diffusion distances that are over five orders of magnitude greater than expected for volume diffusion. This enhanced diffusion is interpreted to represent a combination of fast-diffusion pathways associated with creep cavitation, dislocations and along low-angle boundaries. These new data indicate that ductile deformation localised around inclusions can provide fast pathways for geochemical exchange. These pathways may provide links to the zircon grain boundary, thus negating the widely held assumption that inclusions in fracture-free zircon are geochemically armoured once they are physically enclosed.

1. Introduction

The growth of zircon (ZrSiO₄) from a melt or in metamorphic rocks is commonly accompanied by entrapment or overgrowth of solid mineral phases, melt or fluid inclusions at the migrating zircon/matrix interface. Zircon from a wide range of igneous rock types contains inclusions, that have been used to reveal information about the magma composition from which the zircon grew, temperature conditions during zircon growth, and melt/zircon partition coefficients (Chupin et al., 1998; Danyushevsky et al., 2002;

Li, 1994; Thomas et al., 2003, 2002). The integration of petrological and geochemical studies of the inclusion mineralogy with U–Pb geochronology and trace element geochemistry of zircon permits petrogenetic processes to be placed within an absolute temporal framework. Such an approach can be valuable, for example, in constraining prograde metamorphic pressure-temperature-time paths that are otherwise difficult or impossible to access (Katayama and Maruyama, 2009; Katayama et al., 2002; Liu et al., 2004; Massonne and Nasdala, 2003). Significantly, the ability of zircon to resist chemical and physical breakdown allows old zircons to be used to constrain processes in the early Earth, for example to support the presence of volatile-rich granitoid magmas in the Archaean (Chupin et al., 1998), cool Hadean surface temperatures (Hopkins et al., 2010), and the operation of subduction as far back as 4.25 Ga (Menneken et al., 2007; Nemchin et al., 2008).
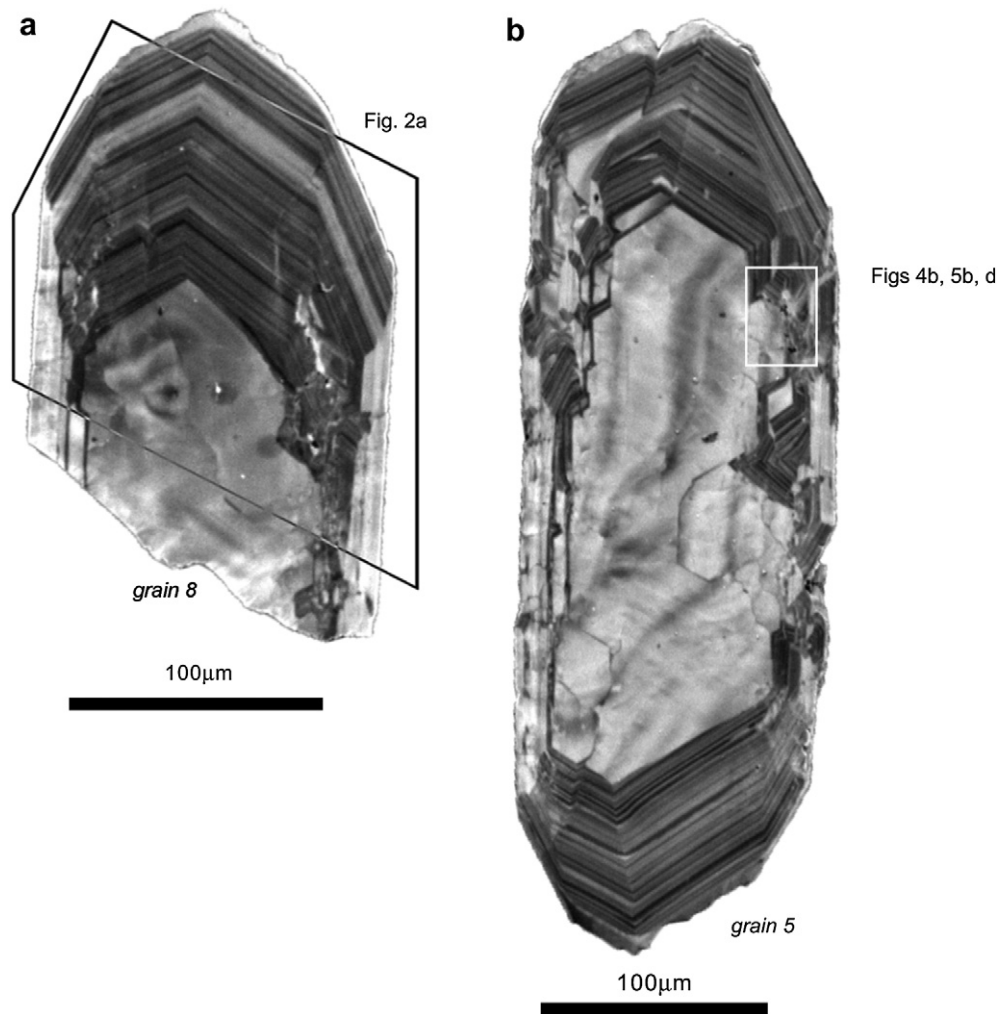
Fig. 1. (a) Panchromatic cathodoluminescence image of zircon grain 8 from the deformed magmatic population from sample Jhs2Pon4 showing cores and oscillatory zoned rim. (b) Panchromatic cathodoluminescence image of zircon grain 5.

Table 1
SEM and EBSD settings and statistics.

Technique	SEM	Detector/acquisition system	Acc. voltage (kV)	Probe current	Working distance (mm)	Tilt (degrees)
PCL	Phillips XL30 (W-filament)	KE developments	10	Spot 7	17.4	0
OCI	Zeiss Neon Dual FIB-FEG	Annular backscatter detector	30	50 pA	4.7–5.4	0
EBSD	Phillips XL30 (FEG)	Oxford instruments channel 5.9	20	Spot 5	20	70
FIB	Helios D433 Dual FIB-FEG	Helios	5/30	16 pA to 9.7 nA	4.5	52
λCL	JEOL 8530F FEG-EPMA	XCLent III	10	10 nA	fixed	0

EBSD settings		Fig. 4a, 5a,c	Fig. 4b, 5b, d		Fig. 6a
EBSP collection time per frame (ms)		60	60		60
Background (frames)		64	64		64
EBSP noise reduction (frames)		4	4		4
(binning)		4 × 4	4 × 4		4 × 4
(gain)		Low	Low		Low
Hough resolution		65	65		65
Match units		Zircon[a]	Zircon[a], magnetite		Zircon[a]
Band detection − no. of bands		8	8		8
Step distance (μm)		0.1	0.1		1
Indexing (percent)		97.14	Zircon: 97.17, magnetite: 0.46		96
Data noise reduction − 'wildspike' removal		Yes	Yes		Yes
- nearest neighbour zero solution extrapolation		5	5		5

[a] generated from zircon crystal structure at 9.8 Atm (∼1 MPa) (Hazen and Finger, 1979).

Critical to the application of mineral and/or fluid inclusions (pores) in zircon to petrogenetic processes is the assumption that the inclusions have been armoured by the zircon and have remained isolated from chemical exchange. Several processes are known to cause the formation of secondary mineral phases and pores in zircon. Hydrothermal alteration of zircon results in migration of reaction interfaces through grains, leaving recrystallised zircon and newly developed pores in their wake (Geisler et al., 2001, 2003). Extreme conditions associated with impacts can lead to phase transformations and decomposition of zircon (Glass et al., 2001; Wittmann et al., 2006). At high shock pressures (>30 GPa), zircon can form microtwins (Leroux et al., 1999; Timms et al., in press) and contain traces of high pressure polymorph reidite,

most commonly as fine-scale epitaxial lamellae (Glass et al., 2001; Leroux et al., 1999). Zircon can also form a granular structure with 'microvesicles' during impact events, and decomposes to baddeleyite and other ZrO_2 polymorphs (Buttermann and Foster, 1967; Wittmann et al., 2006).

The studies of zircon inclusions often assume that the inclusions are chemically isolated from the rock matrix by the armouring characteristics of the zircon host. The justification of this assumption arises from the low diffusivity for volume diffusion of major and trace elements in zircon at crustal temperatures (<900 °C) over geological timescales (Cherniak and Watson, 2003). However, numerous studies have demonstrated that fractures that link the inclusion to the zircon rim allow geochemical exchange between
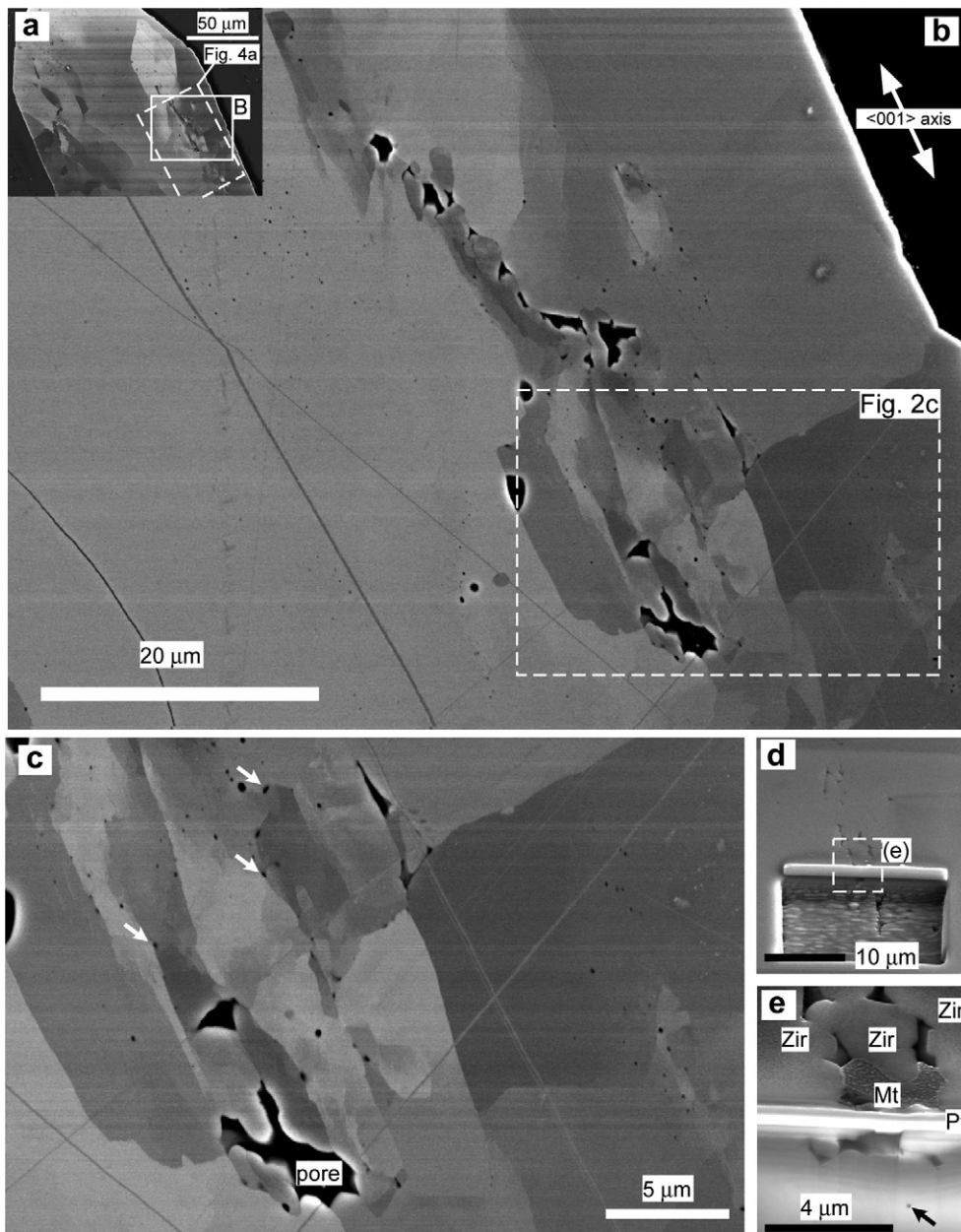
Fig. 2. (a) Orientation contrast image (OCI) of grain 8 showing deformation microstructure. Horizontal stripes are charging artifacts. (b) Detail of area shown in (a). (c) OCI showing deformation microstructure surrounding pores. White arrows highlight sub-micron (type 2) pores along orientation boundaries. (d) Secondary electron (SE) image of the polished surface (oblique view) of grain 5 showing trails of pores and a magnetite inclusion. The rectangular pit in the foreground has been milled using a focused ion beam to a depth of 6.5 μm. (e) Detailed SE image of the mixed magnetite porosity. The lower half of the image shows a vertical cross section through the irregular shaped pore beneath the sample surface. Dark straight lines on (b) and (c) are surface scratches.

inclusion and rock matrix (e.g., Qin, 1992). Inclusions affected in this way can usually be identified since fractures are readily observable by most zircon imaging techniques and can be routinely avoided. More subtle microstructures identified by electron back-scatter diffraction and associated with crystal-plastic deformation of zircon have recently been discovered in a range of geological environments (Kaczmarek et al., in press; Moser et al., 2009; Nemchin et al., 2009; Reddy et al., 2009, 2006; Timms et al., 2006, in press). These microstructures, commonly low-angle boundaries formed by the interaction of dislocations during dislo-cation creep (Reddy et al., 2007), have been shown to facilitate chemical and isotopic exchange between the zircon and the rock matrix (Moser et al., 2009; Nemchin et al., 2009; Reddy et al., 2006; Timms et al., 2006, 2011; Timms and Reddy, 2009) by providing fast-diffusion pathways that increase the bulk diffusivity of the zircon at the grain-scale. Closer examination of deformed igneous zircon grains from a Javanese andesite previously described by Reddy et al. (2009) has revealed that the grains contain fluid and solid mineral inclusions. In this paper, we examine the relation-ships between zircon deformation, recorded by the spatial devel-opment of crystal-plastic microstructures, 'pores' and included mineral phases. We provide the first evidence that primary inclu-sions can localize crystal-plastic deformation in zircon, and demonstrate for the first time that this deformation can be accompanied by the development of new porosity. We confirm that microstructural networks that surround inclusions are fast path-ways for trace element exchange. These observations provide the first examples of alternative pathways for fast-diffusion coupling between inclusion and rock matrix that may sometimes breach the assumption of chemical isolation of inclusion phases.

2. Sample description

The zircon grains used in this study have been described previously (Reddy et al., 2009) and are from an undeformed glomeroporphyritic andesite (Jhs2Pon4) from the boundary between the Southern Mountains Arc and the active Sunda Arc of the Ponorongo region of East Java, Indonesia (7°50′28.8″S; 111°19′45.6″E) (Smyth et al., 2007). The studied rock contains two distinct populations of zircon. One population of zircon grains is undeformed, shows a wide variety of colours (colourless, yellow, brown) and sizes (100–300 μm long) and shapes (rounded to subhedral), records a range of Archaean to Cambrian ages and is interpreted to be xenocrystic (Reddy et al., 2009). The grains of the second population are 150–500 μm long, euhedral orange crystals, which show complex oscillatory zones in cathodoluminescence images (Fig. 1) and preserve uniform U–Pb ages with a mean age of 9.28 ± 0.21 Ma (Reddy et al., 2009). These grains are interpreted to be 'magmatic' and petrogenetically related to the andesite (Reddy et al., 2009). Approximately 80% of the magmatic grains preserve crystal-plastic deformation microstructures and spatially-associated disrupted cathodoluminescence properties (Reddy et al., 2009; Timms and Reddy, 2009). These deformation micro-structures are best seen in orientation contrast images (OCI), electron backscatter diffraction (EBSD) and hyperspectral cath-odoluminescence (CL) maps, yet are cryptic in panchromatic CL images and not apparent via optical microscopy (Timms and Reddy, 2009). The deformation of these zircon grains is interpreted to have taken place within a low-melt fraction adcumulate stage of a crys-tallizing magma in the mid- to lower crust (Reddy et al., 2009). Disaggregation of this cumulate and remobilization by a second melt phase resulted in melt migration through the crust, xenocryst scavenging and emplacement of the andesite at shallow crustal levels. This study examines porosity and inclusion-related micro-structures within this younger population of zircon grains.

3. Analytical techniques

The separation of zircon from the sample, and details of the mounting and polishing procedures and cathodoluminescence imaging have been presented in detail elsewhere in Reddy et al. (2009). Orientation contrast imaging was performed on polished sections of the grains as a rapid means of providing qualitative microstructural information (e.g., Lloyd, 1987), and were acquired using a Zeiss Neon 40 dual beam focused ion beam (FIB) field emission gun (FEG) SEM at Curtin University. Orientation contrast was achieved on untilted samples using an annular backscattered electron detector and reduction of the working distance to ∼5 mm, and, thus increasing the effective take-off angle of backscattered electrons. This technique is an alternative to the forward-mounted detectors used for simultaneous OCI and EBSD mapping (e.g., Prior et al., 1999), that overcomes problematic shadow effects from detection from a limited range of angles.

Quantitative microstructural data were collected via EBSD mapping undertaken on a Phillips XL30 FEG SEM fitted with an Oxford Instruments EBSD acquisition system, based at Adelaide Microscopy, University of Adelaide, South Australia. SEM and EBSD settings were optimized for zircon after Reddy et al. (2007) and Reddy et al. (2008), and are given with EBSD indexing statistics in Table 1. All EBSD data were processed using Oxford Instruments Channel 5 (SP9) software using procedures detailed elsewhere (Reddy et al., 2007). EBSD data were used to generate orientation maps, crystallographic pole figures and misorientation axis distri-butions. Details of these plotting procedures have also been described elsewhere (Reddy et al., 2007).

Focussed ion beam milling was used to prepare samples for transmission electron microscopy (TEM) and provided an assess-ment of the microstructural geometry in three dimensions. FIB-milling was done using an FEI Helios DualBeam FIB-SEM D433 at Adelaide Microscopy, University of Adelaide, using settings given in Table 1. The FIB-milling procedure involved deposition of a protec-tive platinum strip (2 μm wide × 1 μm deep), then 'rough' milling a rectangular trench at 30 kV and 21 nA probe current, and 9.3/2.8 nA to reduce milling artefacts. The vertical trench wall was then given a 'fine' mill at 30 kV and 9.3 nA to reduce ion damage and secondary deposition. Secondary electron images were taken using an electron beam at 20 kV and 21 pA/0.17 nA current. TEM foils were prepared following the same procedure but with a wedge cut symmetrically either side of the platinum strip. The region of interest was then milled from the sample (30 kV beam and 2.8 nA
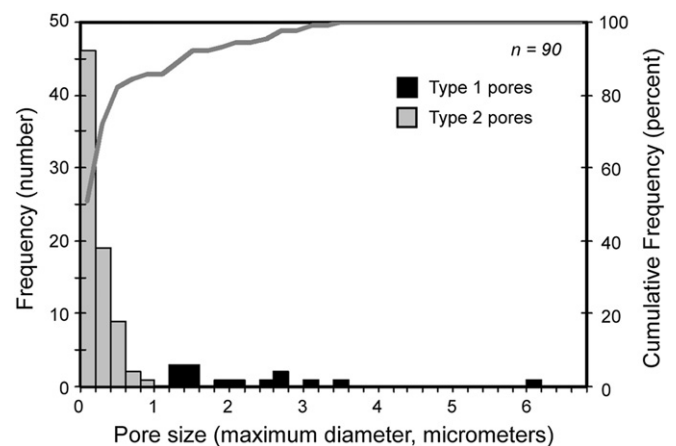

Fig. 3. Pore size distribution. Data represents the maximum diameter of pores measured from an orientation contrast image of an area of grain 8 shown in Fig. 2b.

current), picked up and welded (30 kV beam and 9.7 nA current) to an Omniprobe TEM grid within the SEM via a micro-manipulator, and thinned to ~500 nm on both sides using a 2.8 nA beam, then further using a 48 pA beam. The foil surfaces were 'cleaned' using 5 kV, 16 pA beam at ±8° tilt for 5 min each.

TEM imaging and diffraction was conducted using a Philips CM300T instrument at the Australian National University in Canberra. The instrument was operated at 300 kV and images recorded

via a Gatan MSC 794 digital camera. The FIB-prepared foils were manipulated in the TEM using a conventional double-tilt specimen holder.

Hyperspectral cathodoluminescence data were collected using a 2049-element linear spectrometer/CCD-Si mounted on a JEOL 8530F FEG electron microprobe in the Centre for Microscopy, Characterisation and Analysis at the University of Western Australia, Perth. Probe conditions were optimized for spatial resolution
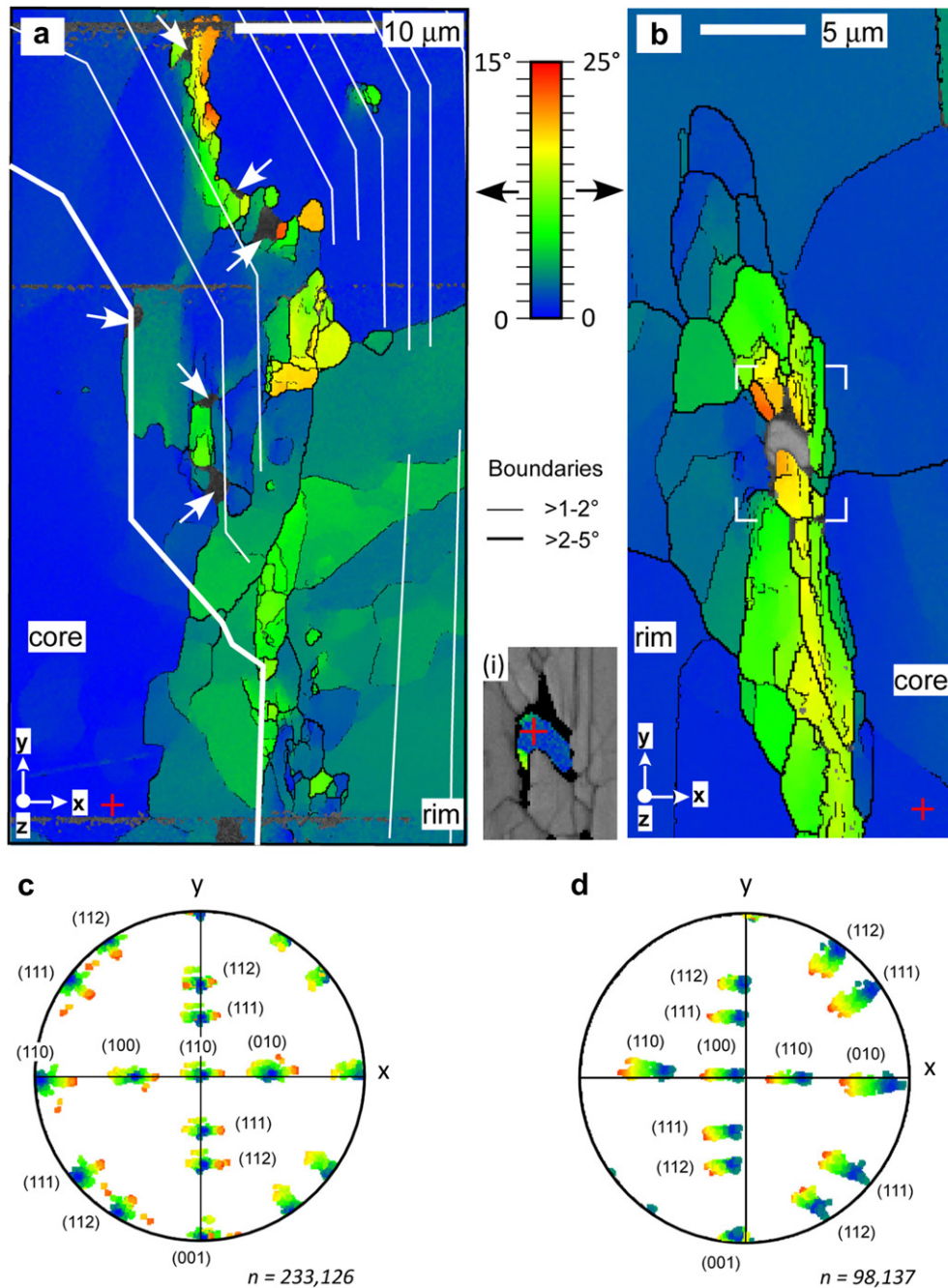
Fig. 4. (a–b) Orientation maps from electron backscatter diffraction data for grains 8 and 5, respectively. Coloured for cumulative crystallographic misorientation (in degrees) from orientation at a reference point (indicated by red cross). The locations of type 1 pores are indicated by white arrows. The trace of CL zoning is shown by white lines. Horizontal features are artifacts of beam scanning in the SEM. (b) Shows microstructure surrounding a magnetite inclusion. Orientation boundaries are shown as black lines. Inset (i) shows cumulative misorientation (5°) across the magnetite inclusion in (b). Step size for maps is 0.1 μm (a) contains 233126 data points, (b) contains 98137 data points. (c–d) Pole figures of the low-index crystallographic axes in zircon for every data point shown in maps (a) and (b), respectively. Colour scheme as in (a) and (b). The (001) poles cluster in both (c) and (d), and the domination by one colour is because all axes plot on top of each other in the plot, so are dominated by the last points in the plot sequence. In contrast, the systematic colour dispersion on small circles for all other axes indicates these are all rotated around the c-axis. Pole figures are lower hemisphere, equal area projections. (For interpretation of the references to colour in this figure legend, the reader is referred to the web version of this article.)

with 10 kV accelerating voltage and 10 nA probe current. Spatial resolution at these conditions is approximately 1 μm. Automated mapping involved the collection of CL spectra in 196−903 nm wavelength range on a user defined grid with node spacing of 300 nm. Dwell times per point of 800 ms were used to achieve an acceptable signal to noise ratio. Hyperspectral CL data were processed using xCLent III software (MacRae et al., 2005). Trichromatic maps were produced by assignment of three colour channels to wavelength ranges that define the dominant peaks in CL emission. Mean CL spectra for regions of interest on the map are presented as raw counts and normalized to a spectrum from the zircon core for the purpose of comparison.

4. Results

Orientation contrast imaging shows that over 75% of the zircon grains from the 9.3 Ma population contain lattice orientation variations that occur throughout the grains and are not limited to just grain edges (Fig. 2). In all cases, orientation variations are most commonly manifest by discrete, polygonal boundaries, with relatively few domains of gradational change. These deformation microstructures cross cut primary growth zones seen in CL images (Figs. 1 and 2). Orientation boundaries and, more commonly, their triple junctions are decorated with type 2 pores. Orientation domains are commonly curved, yet; the trace of the boundaries visible on the prepared surface of the zircon are predominantly aligned parallel to the c-axis of the grains (Fig. 2b, c).

Pores occur throughout all of the 9.3 Ma igneous zircon grains, and form two distinct groups based on their size and shape characteristics. The larger pores (type 1 pores) are approximately 1−7 μm across, have irregular cuspate shapes with concave walls, and occur in the oscillatory-zoned rims of the grains (Figs. 2 and 3). Magnetite (Fe_3O_4) inclusions, typically 1−3 μm across, are sometimes found within type 1 pores (Figs. 2e and 4b). Smaller pores (type 2 pores) are much more numerous (>80% by frequency), are typically 100−400 nm across, have simple shapes with low aspect ratios, and typically occur in clusters and trails in the vicinity of larger pores (Figs. 2 and 3). Like the larger pores, these cavities have cuspate margins with pointed edges and terminations. 3D analysis of the pore space (Fig. 2c, d) by focussed ion beam milling shows that type 1 and type 2 pores extend beneath the sample surface and are not formed by the plucking out of material during polishing. There is no evidence of melt in the magnetite inclusions or pores.

EBSD orientation maps show changes in lattice orientation across the grain accommodated by orientation boundaries with 1−20° misorientations, or 'low-angle boundaries' (Figs. 4 and 5) with the most complex and intensely developed microstructures being proximal to the type 1 pores and mineral inclusions. Low-angle boundaries delimit domains with little orientation variation, or 'subgrains' (Reddy et al., 2009). Grain 5 contains a complex, irregular type 1 pore that also contains a microcrystal of magnetite. The magnetite has curved interfaces with the pore and host zircon, and preserves intragrain crystallographic misorientation of up to 5° accommodated by a low-angle boundary (Fig. 4b). The magnetite-pore 'inclusion' is surrounded by low-angle boundaries that define an ellipsoidal zone of subgrains around the microcrystal of magnetite (Fig. 4b). The long axis defined by the network of subgrains is within 10° of the c-axis of the grain. The network of low-angle boundaries link pores and inclusions with the grain boundary of the zircon (Figs. 2 and 4).

EBSD data show the dispersion of lattice orientations (Fig. 4c, d) and the majority of low-angle misorientation axes (Fig. 5) are subparallel to <c> of the zircon grain. Some low-angle boundaries have misorientation axes that lie parallel to the a-planes or coincide with other low-index crystallographic directions (Fig. 5). These boundaries are interspersed throughout the deformation microstructure, and do not show systematic relationships with strain intensity or position relative to pores (Fig. 5).

TEM foils were made across boundaries with different boundary plane - misorientation axis relationships to determine the nature of the slip systems in different boundary geometries (Fig. 6a). TEM analysis shows that all of the lattice misorientation in these domains occurs at the boundaries with almost no free dislocations within subgrains (Fig. 6). Black spots visible in the TEM images represent nano-sized regions where the crystal has some local point imperfection resulting in a small surrounding zone of elastic lattice strain. These regions diffract differently to the surrounding unstrained crystal, hence they appear darker in these brightfield TEM images. The nature of the imperfections was not established and they may have more than one origin. Their likely causes include nano-sized inclusions, centres of natural radiation damage or artefacts of FIB milling.

A low-angle (∼1.4°) boundary shows strain indicating that it is accommodated by necessary dislocations (Fig. 6d). This boundary has local variations in orientation and is approximately parallel to (110). A boundary with 3.5° misorientation around <c> also has local variation in the orientation of the boundary plane at the TEM scale, and locally parallel with (011) and (001) (Fig. 6f, g). Periodic contrast (ledges?) can be seen along the boundary at around 20 nm spacing and are inconsistent with a perfect twist boundary of [100] + [010] screw dislocations with [001] twist axis and Burgers' vector magnitude of 6 Å because dislocations in each set would be spaced apart by ∼10 nm for a 3.5° misorientation through geometric necessity (Fig. 6f, g).

A boundary with ∼4° misorientation around <c> shows periodic contrast at 10−15 nm scale, no free dislocations, has a variable boundary orientation and is faceted at the 100−250 nm scale (Fig. 6e). Here the longest facets lie near (010) and could be arrays of edge dislocations with [010] Burgers' vector and slip plane (100), as such could be pure tilt segments. However, the intervening facets are not well defined and the majority of the boundary is not of this type. A boundary with 16° misorientation around <c> is curved and has no sign of dislocation contrast (Fig. 6 d).

Hyperspectral CL mapping shows that the oscillatory growth zoning pattern in the rim and the relatively homogeneous core zones are superimposed by networks of bands and patchy domains with significantly different CL characteristics to the host zircon, seen as orange-yellow areas on Fig. 7a. These CL patterns spatially coincide with the low-angle boundary and subgrain microstructures identified by orientation contrast imaging and EBSD mapping (Figs. 2−5). Significantly, these microstructures cross cut primary growth zoning in the core and oscillatory zoned rim, and connect type 1 pores with the zircon grain boundary (Fig. 7a). Analysis of the CL spectra shows three dominant broad peaks at ∼400, ∼475 and ∼525 nm, with narrow peaks superimposed at many different wavelengths (Fig. 7b). Normalization of spectra from different parts of the zircon to that of the homogeneous core permits a comparison of the intensity of the emission wavelengths relative to the core (Fig. 7c). The brighter parts of the oscillatory zoned rim has relatively more intense luminescence in 315−460 nm range with peaks at 350, 380 and 405 nm, and relatively less luminescence in the 460−680 nm range with troughs at 470, 520 and 570 nm (Fig. 7c). The spectrum from the darker unaltered banded area has lower CL signal, and lower peaks in the 350−780 nm range relative to the core (Fig. 7c). Spectra from the darker banded domains have more similarities in shape to the bright parts of the rim (area 1 in Fig. 7) than the core (area 4 in Fig. 7). Poor signal in these low-luminescent areas has resulted in significantly lower signal to noise ratio than in normalised spectra from strongly luminescent areas (Fig. 7c). Spectra from two 'altered' domains show a different pattern from
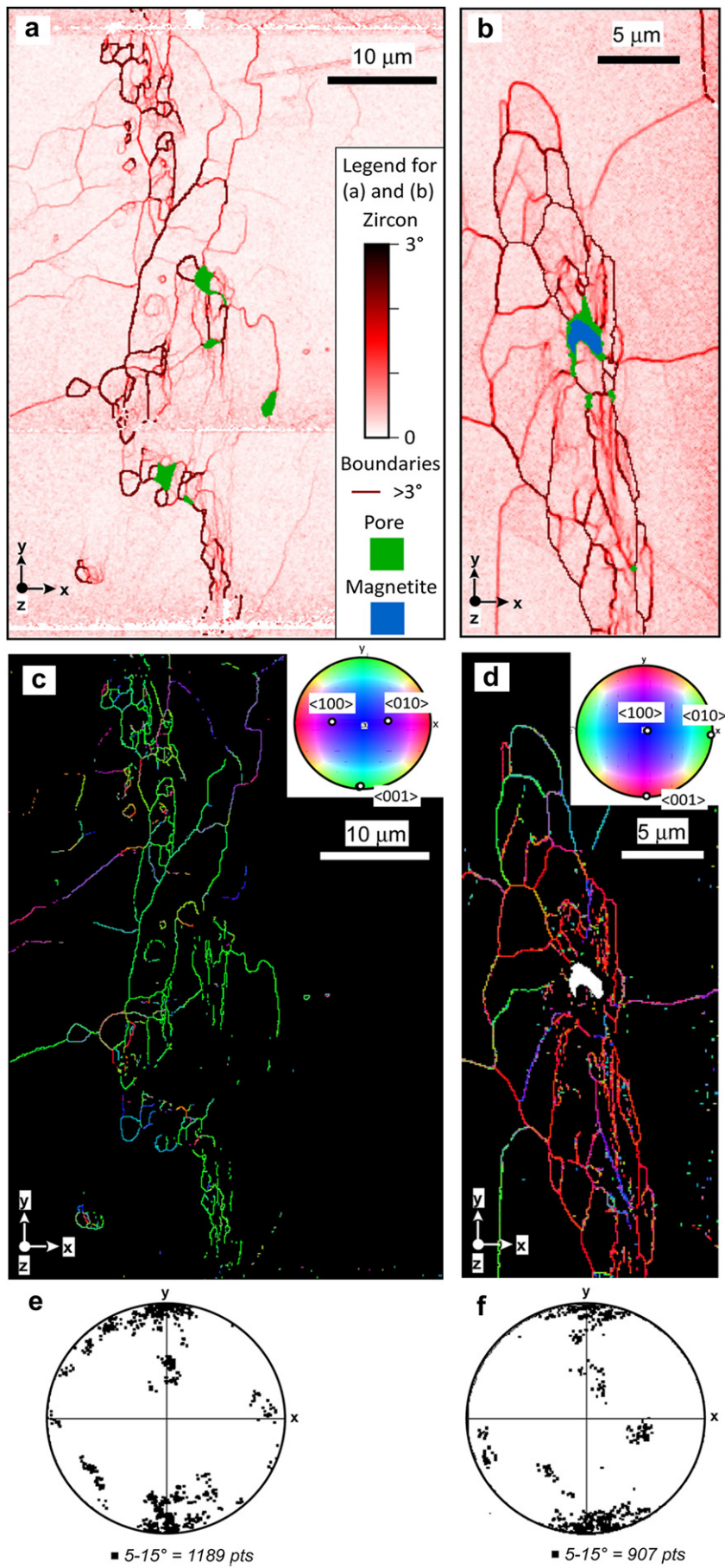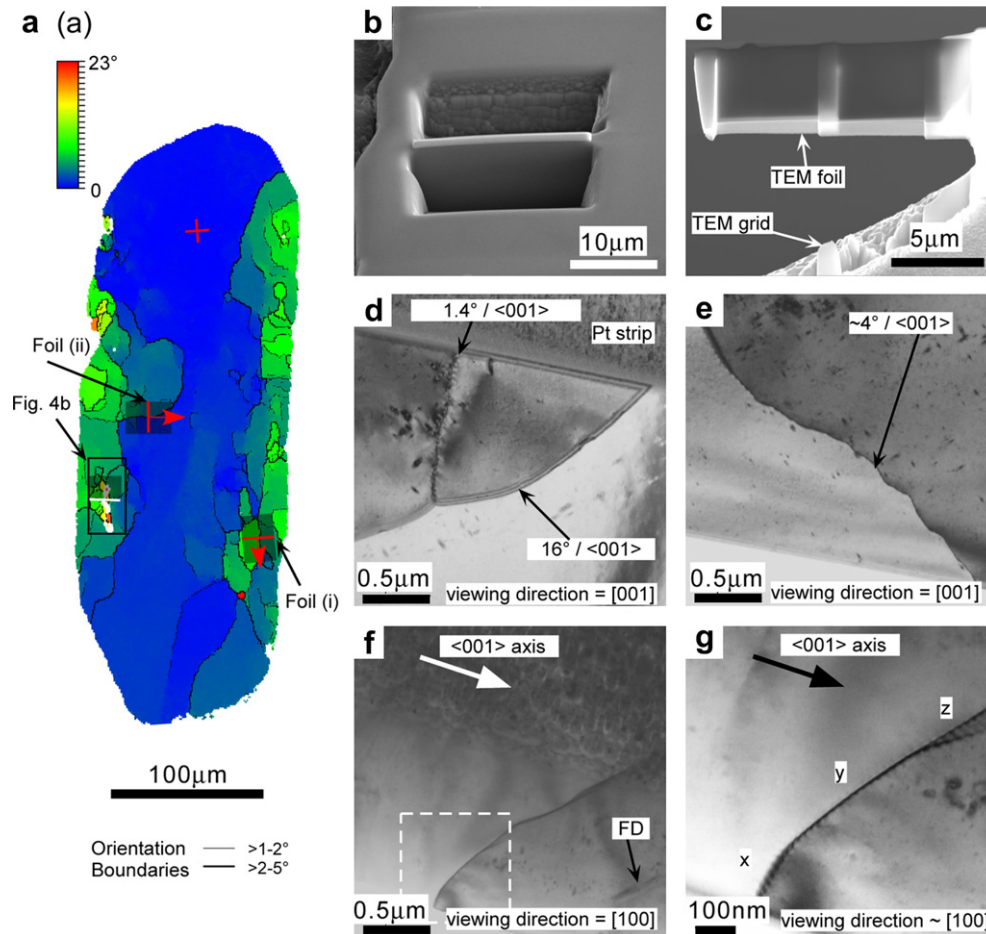
Fig. 6. (a) EBSD map of grain 5 showing the location of FIB-milled TEM foils. (b) SE image of *in situ* region of interest for TEM foil (i) during FIB milling preparation. (c) Thinned TEM foil (i) attached to TEM grid. (d) TEM image from foil (i) of two boundaries with different misorientation axes around <c>. Strain can be seen associated with dislocations in the 1.4° boundary. (e) TEM image of a 4° boundary in foil (i). (f) and (g) images of a boundary in foil (ii). (f) A rare free dislocation (FD) can be seen in the far right. (g) A detail of the area shown by the white box in (f). The boundary plane changes orientation from ~(001) at x to ~(011) at point z and is aligned with the viewing direction at point y. Periodic contrast can be seen along the boundary at ~20 nm spacing. Viewing direction for (f) and (g) is ~5° from [100]. Black spots in TEM images are either nano-scale inclusions, centres of natural radiation damage or artefacts of FIB milling.

the core and rim spectra and have relatively less emission in the 315–485 nm range with troughs at ~345, 382, 405 and 470, and relatively stronger emission from 485 to 700 nm with peaks at 512, 548, 559 and ~587 nm (Fig. 7c).

5. Discussion

5.1. Deformation mechanism of zircon

The development of low-angle boundaries, subgrains, and progressive changes in crystallographic orientation with rational, low-index misorientation axes is consistent with deformation by the formation and migration of dislocations. The predominance of low-angle boundaries suggests that dislocation glide and climb

were operational to accumulate dislocations into subgrain boundaries whilst leaving the subgrain interiors without free geometrically necessary dislocations. Such dislocation creep microstructures are usually indicative of high temperature creep in other minerals (e.g., Hirth and Tullis, 1992). Zircon deformation took place due to tectonic stresses within a low-melt fraction (\5% melt), mid-lower crustal cumulate prior to magmatic disaggregation and ascent to higher crustal levels in the Sunda Arc (Reddy et al., 2009). The trend of crystallographic misorientation axes associated with low-angle boundaries and the trace of the low-angle boundary on the sample surface can be used to determine the dominant dislocation slip system responsible for the low-angle boundary by using simple geometric models (Boyle et al., 1998; Prior et al., 2002; Reddy et al., 2007). The data are consistent with 'tilt' and 'twist' boundaries,

Fig. 5. (a) and (b) Maps to show the local gradients in crystallographic misorientation within deformed regions around inclusions in grains 8 and 5, respectively. Each pixel is coloured for the mean misorientation with its immediate neighbouring analytical points (i.e., a local 3 × 3 pixel grid). Units are degrees per 0.3 μm. Subgrain boundaries between adjacent pixels with a crystallographic misorientation greater than 3° are shown as solid maroon lines. Non-indexed points that coincide with pores are shown in green, and other non-indexed points are white. Magnetite inclusion in (b) is shown in blue. (a) and (b) show that the microstructures predominantly consist of low-angle (<10°) subgrain boundaries. Horizontal features in (a) are artifacts of beam scanning in the SEM. (c) and (d) Maps showing >1° subgrain boundaries coloured for misorientation axis direction relative to the sample x-y-z reference frame for grains 8 and 5, respectively. Boundaries are assigned colours based on the scheme shown in the lower hemisphere equal area projection legend such that steeply plunging misorientation axes are blue, and shallowly plunging misorientation axes are red/yellow/green. The mean orientation of the grain is shown by the low-index directions superimposed on the legends. Note: the difference in the colour scheme for (d) is because the map has been rotated 90° from the orientation of data acquisition so that <c> is (sub)parallel to y. (c) and (d) show that c-axis-parallel misorientation axes are the most prevalent. (e) and (f) are equal area lower hemisphere projection of misorientation axis trends for 5–15° low-angle boundaries shown in (c) and (d), respectively. (For interpretation of the references to colour in this figure legend, the reader is referred to the web version of this article.)

where the misorientation axes are parallel with and perpendicular to the low-angle boundary surfaces, respectively. The majority of the low-angle boundaries have misorientation axes that cluster at or near the zircon c-axis direction (Fig. 5c, d). The variable orientation of these boundaries suggests that their formation is dominated by the accumulation of varying combinations of either screw and/or edge dislocations, including dislocations with one of the two symmetrically equivalent <100> Burgers vectors. This supports findings from other studies that indicate that the <100>{010} slip system is common in crystal-plastically deformed zircon (Leroux et al., 1999; Moser et al., 2009; Nemchin et al., 2009; Reddy et al., 2009, 2007; Timms et al., 2006, Timms et al. 2011). The small number of low-angle boundaries with non-c-axis-parallel misorientation axes are a consequence of various degrees of mixing between <100>{010} and <001>{100} slip, and/or the activity of higher order slip systems. Very few of the boundaries seen with TEM in the FIB foils have pure tilt or twist character. In fact, the variation of angle between misorientation axis and boundary-plane normal by over 90° for most low-angle boundaries indicates an overall lack of either dominant tilt or twist geometries (Fig. 5c, d).

5.2. Origin of type 1 pores and inclusions

It has been demonstrated that brittle fracture can precede and facilitate ductile deformation (and eventually recrystallisation at higher strains) of quartz, feldspar and olivine (Cordier and Doukhan, 1989; Gerald et al., 1991; Green II and Gueguen, 1983; Stünitz et al., 2003; Trepmann and Stöckhert, 2003; Vernooij et al., 2006). In these studies, dilatation and healing of fractures led to the development of trains of fluid inclusions with cuspate boundaries along the traces of fracture planes. In this study the type 1 pores show no evidence of fracture-related crystallographic misorientation or systematic trains of inclusions, such as would be expected at dilatational jogs along stepped or intersecting fracture planes, newly grown (healed) zircon or fracture traces in CL images. It is therefore unlikely that type 1 pores represent secondary fluid inclusions associated with healed fractures. The clustering and intimate relationship between type 1 pores and mineral inclusions along similar growth zones indicates that type 1 pores represent 'primary' fluid inclusions trapped during the crystallization of zircon from melt. Therefore, type 1 pores are trapped bubbles of
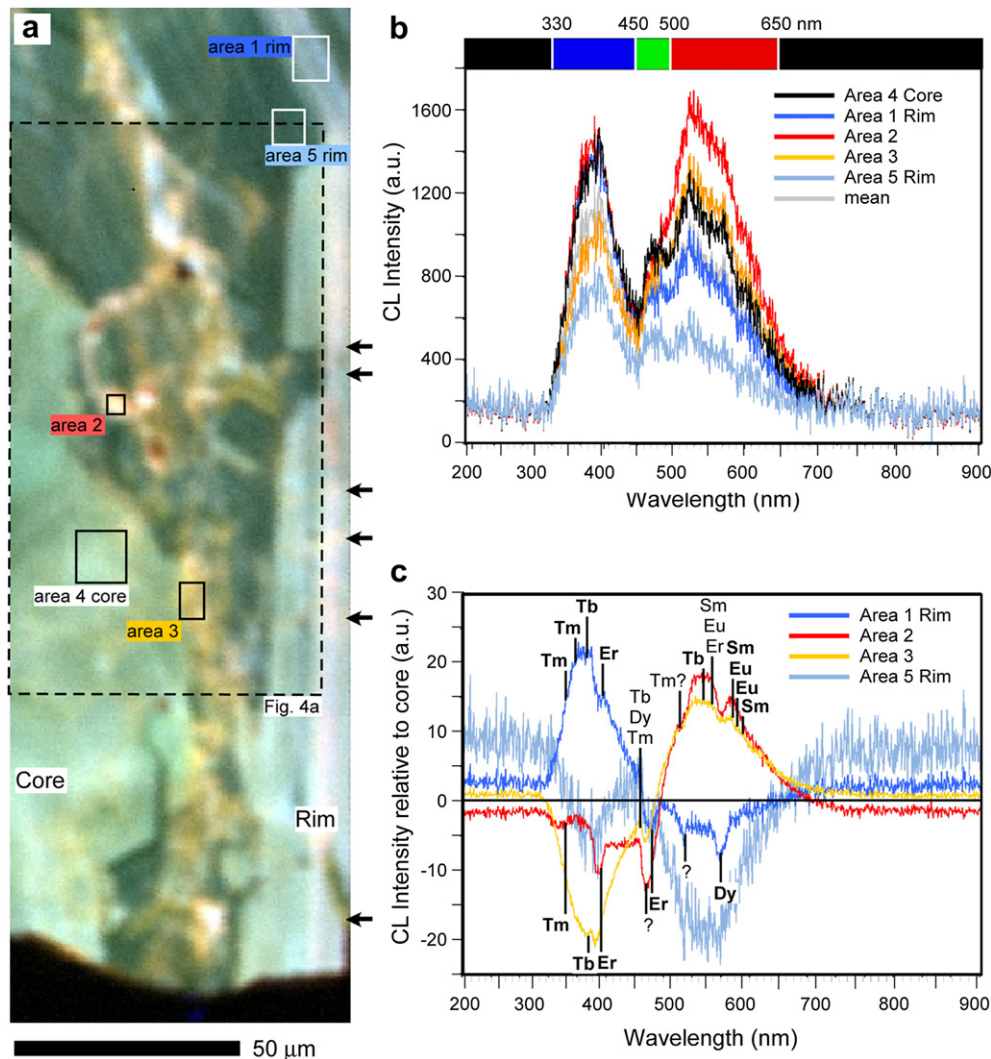
Fig. 7. Hyperspectral CL data from a deformed area of grain 8. (a) False colour hyperspectral CL map. Blue, green and red channels assigned to 330–450 nm, 450–500 nm and 500–650 nm ranges, respectively. Colour change from blue-green to yellow-orange indicates a relative increase in CL emission in the 450–650 nm range. Black arrows indicate where low-angle boundaries connect with the zircon grain boundary. (b) Mean CL spectra from whole map and numbered areas shown in (a). Vertical axis shows total signal in arbitrary units (a.u.). (c) CL spectra from (a) normalized to core spectra showing changes in CL emission relative to the core spectra. Vertical axis shows signal relative to that of area 4 shown in (a), in arbitrary units (a.u.). The positions of dominant peaks for CL-active REE in the emission region of interest are labeled. REE peak data from Blanc et al. (2000) and Gaft et al. (2000). (For interpretation of the references to colour in this figure legend, the reader is referred to the web version of this article.)

a co-magmatic fluid phase, such as CO_2, H_2O or CH_4-rich fluids, and inclusions of microcrystalline magnetite.

5.3. Dynamic generation of type 2 porosity by 'creep cavitation'

The type 2 pores lie at the triple junctions of the subgrain boundaries and, less commonly, along low-angle boundaries (Fig. 2b, c). The occurrence of sub-micron pores at subgrain boundary triple junctions and boundaries (e.g., Fig. 2b, c) is strong evidence of cavitation caused during dislocation creep in zircon (Fig. 8). It is has been proposed that during dislocation creep, nanometer-scale cavities, known as Zener-Stroh cracks, accumulate at grain boundaries and triple junctions by dislocation pile-ups (Stroh, 1957; Weertman, 1986). Weertman (1986) suggested that two or more edge dislocations sliding on a single plane could coalesce into a newly opened space (effectively a nano-size crack) so that then becomes the nucleus of a Zener-Stroh macro-crack. As such, tubule-shaped cavities tend to form parallel to dislocation lines at low-angle boundaries. The cavities at triple junctions can be caused by the coalescence of dislocations pile-ups on more than one intersecting slip plane (Cottrell, 1958). Cavitation of high-angle grain boundary triple junctions is usually a sign of grain-boundary sliding. However, this deformation mechanism is unlikely because the triple junctions are for low-angle boundaries and the bulk strain in the grains is clearly very small. Vacancy agglomeration could also contribute to cavitation at boundaries (Raj and Ashby, 1975). This mechanism of void growth involves the condensation of vacancies along boundaries via diffusion, a process that becomes more important with increasing temperature conditions (Kassner and Hayes, 2003). The size of Zener-Stroh cavities is a function of the local low-angle boundary orientations, the dislocation slip systems that contributed to their development, and the total misorientation in the vicinity of the triple junction (Dyson, 1983; Westwood et al., 2004). However, type 1 pores do not show a relationship between the magnitude of local misorientation or boundary geometry with pore size (Fig. 5), and are inconsistent with a creep cavitation origin, which is in agreement with a primary inclusion origin for type 1 pores.

5.4. The relationship of type 1 pores and mineral inclusions with the deformation microstructure

Type 1 pores and mineral inclusions are surrounded by crystal-plastic microstructures, recognized by EBSD mapping. It has been demonstrated that dislocation-related defects, such as low-angle boundaries, can nucleate at irregularities on crystal interfaces, such as inclusions, and propagate during mineral growth (Bestmann et al., 2005; Timms et al., 2009). The distribution of defects around type 1 pores and mineral inclusions is relatively symmetric (prolate) and not related to the direction of crystal growth. This eliminates the possibility that the crystal defects nucleated at the zircon-inclusion interface during growth. Furthermore, the deformation microstructures cross cut growth zoning in the cores and rims. Therefore, the microstructures must have localised around the type 1 pores and mineral inclusions after the zircon had grown. This is supported by the fact that the magnetite grain also preserves crystal-plastic deformation microstructures (Fig. 4b).

The nature of the interaction between localised inclusion-related stress and the anisotropic properties of zircon are unknown. However, the pseudo-elliptical (ellipsoidal in 3D?) pattern of plastic strain around the magnetite inclusion may represent the ductile response to localised stress perturbations with a similar geometry to that of the enveloping elastic field developed around a pre-existing inclusion (Eshelby, 1959; Healy,

2009; Nasdala et al., 2005). The patterns of deformation microstructures around inclusions also have some similarities to those observed around mineral inclusions in diamonds that result from stresses that arise from relative volume changes during exhumation from the lower mantle (Cayzer et al., 2008). However, in this study deformation-related microstructures are prevalent away from inclusions, indicating that tectonic stresses were sufficient for zircon deformation without requiring stresses associated with volume changes (Reddy et al., 2009). The data presented here show that the presence of type 1 pores and mineral inclusions in zircon can localize crystal-plastic deformation within the interior of grains and not necessarily just at the edge of grains.

The minimization of surface energy during entrapment of primary fluid inclusions would have resulted in simple sub-spherical pore geometries (e.g., Corfu et al., 2003; Thomas et al., 2003)(Fig. 8). Therefore, the complex concave walls of the large pores (e.g., Fig. 2b, e) suggest that the zircon-pore interfaces have been modified (Fig. 8).
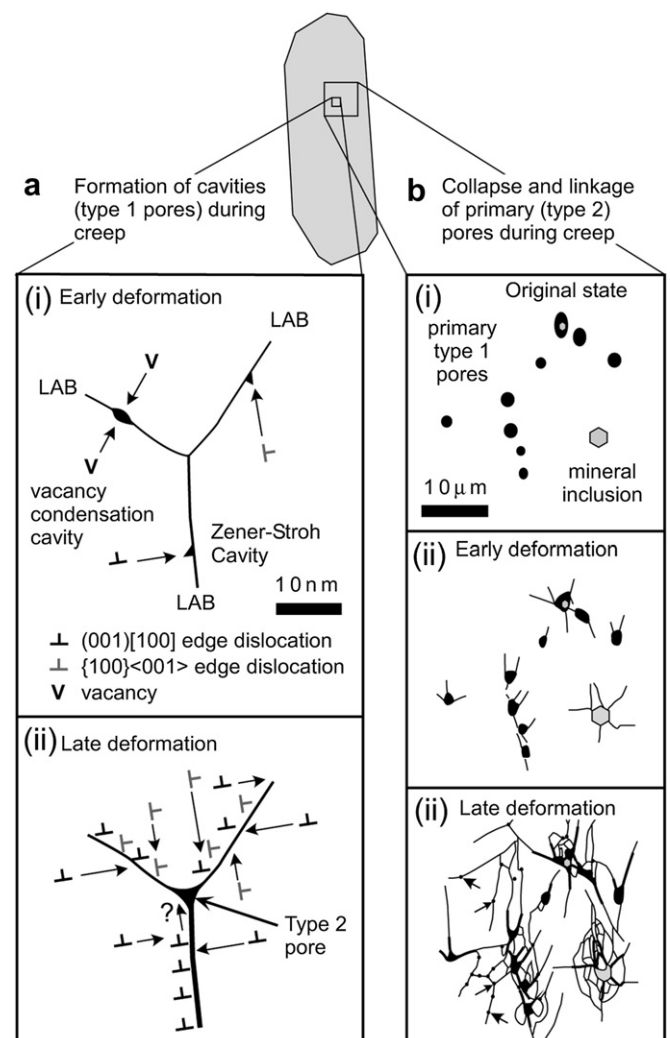
Fig. 8. (a) Conceptual diagram to show the formation of cavities during creep. (i) Formation of cavities along low-angle boundaries (LAB) by Zener-Stroh and vacancy diffusion mechanisms. Dislocations and vacancies migrate into LABs during dislocation creep. (ii) Coalescence of cavities at triple junctions to produce type 2 pores. (b) Diagrams to show the evolution of microstructures around primary (type 1 pores) and mineral inclusions in zircon. (i) Initial state involves strain-free zircon and various inclusions. (ii) Initiation of deformation results in localized lattice strain around inclusions. (iii) As deformation progresses, low-angle boundaries connect in networks, new subgrains form, and pore walls become concave.

It is plausible that the type 1 pores have undergone limited shape modification by Zener-Stroh mechanisms. However, the highly irregular type 1 pore shapes require other deformation mechanisms, such as mass transfer accommodated boundary migration, or surface energy driven grain boundary bulging of zircon into the pore spaces. These processes require that either the pore-filling phase was compressible or has 'leaked' from the pores during deformation. If the latter is true, then the relatively disordered structure and Zener-Stroh cavities of low-angle boundaries are the most likely pathways for leakage from pores in the grains.

5.5. The relationship between rare earth element composition and deformation microstructure

Hyperspectral CL mapping shows a link between the deformation microstructure and altered CL response (Fig. 7). It is well established that the main cause of cathodoluminescence of zircon is the incorporation of trivalent rare earth elements (REE^{3+}) into the zircon structure (Blanc et al., 2000; Cesbron et al., 1995; Nasdala et al., 2002, 2003; Remond et al., 1992). Individual REE^{3+}s cause emission over several specific narrow wavelength ranges, or 'bands', commonly with one or two dominant bands (Blanc et al., 2000; Gaft et al., 2000). The sum of all emission bands gives the shape of the CL spectra and the integrated intensity seen in panchromatic CL images (Fig. 1). Therefore, the CL spectra from grain 8 can be interpreted in terms of contributions of luminescence from a variety of REE^{3+}, the dominant peaks of which are annotated on Fig. 7c. In studies where REE concentrations have been measured by ion microprobe, CL peak intensity generally corresponds to REE concentration in deformed zircon (e.g., Reddy et al., 2006). However, the microstructures and associated alteration domains in this example are much finer than the diameter of an ion microprobe analysis spot (SHRIMP = 20 μm), and preclude ion microprobe calibration of the hyperspectral CL data due to problems associated with volume averaging in the analytical spot. Furthermore, overlaps of minor peaks from different REE^{3+} and poorly understood effects of other defects (e.g., OH^- defects and radiation damage) negate reliable deconvolution of hyperspectral CL data for REE^{3+}. Nevertheless, dominant peaks observed in the normalized CL spectra correspond closely with REE^{3+} peaks. Changes in the relative peak intensities are interpreted to be related to changes in the relative concentration of different REE^{3+} such that light to middle REE (Pr, Sm, Eu) are relatively enriched over middle to heavy REE (Tm, Er, Dy, Tb) in the vicinity of low-angle boundaries (Fig. 7b). This is consistent with the links between crystal-plasticity, CL and REE in zircon reported elsewhere (Reddy et al., 2006; Timms et al., 2011; Timms and Reddy, 2009), and implies open system REE exchange between zircon and an external source.

5.6. Fast pathways for element exchange during ductile deformation in zircon

The crystallization U–Pb age of 9.28 ± 0.21 Ma for the population of zircon grains obtained by Reddy et al. (2009) places upper bounds for the temperature-time history of these grains. The grains must have remained closed to Pb diffusion since their crystallization, and so cannot have been above ~800–850 °C (Cherniak and Watson, 2003). Simple modelling for these temperature and time conditions shows that the distances over which REE modification is observed in these grains (~50 μm) is at least five orders of magnitude more than that expected for volume diffusion (assuming a spherical geometry and diffusion parameters of Cherniak et al. (1997). Therefore, this study identifies that dislocations and low-angle boundaries, spatially associated with inclusions, provide fast-diffusion pathways that link inclusions to the grain boundary

network. Furthermore, dynamic development of new porosity along low-angle boundaries by dislocation creep cavitation represents a previously unrecognized type of fast-diffusion pathway in zircon. So-called 'creep cavitation' has been identified as a potentially important mechanism for the generation of permeable pathways in metamorphic rocks (Delle Piane et al., 2009; Fusseis et al., 2009; Mancktelow et al., 1998; Rybacki et al., 2008). Crystal plastic deformation around inclusions may therefore facilitate modification of inclusion chemistry, thereby negating the assumption of inclusion armouring by the host zircon. The presence of pre-existing pores and inclusions can locally enhance plastic deformation because they are stress risers within zircon, and could localize plastic strain of the surrounding zircon. Fluids from within pores could facilitate mass transfer along deformation-related defects in zircon.

Acknowledgements

References

Bestmann, M., Piazolo, S., Spiers, C.J., Prior, D.J., 2005. Microstructural evolution during initial stages of static recovery and recrystallization; new insights from in-situ heating experiments combined with electron backscatter diffraction analysis. Journal of Structural Geology 27 (3), 447–457.

Blanc, P., Baumer, A., Cesbron, F., Ohnenstetter, D., Panczer, G., Rémond, G., 2000. Systematic cathodoluminescence spectral analysis of synthetic doped minerals: anhydrite, apatite, calcite, fluorite, scheelite and zircon. In: Pagel, M., Barbin, V., Blanc, P., Ohnenstetter, D. (Eds.), Cathodoluminescence in Geosciences. Springer-Verlag, Berlin, pp. 127–160.

Boyle, A.P., Prior, D.J., Banham, M.H., Timms, N.E., 1998. Plastic deformation of metamorphic pyrite: new evidence from electron backscatter diffraction and forescatter orientation-contrast imaging. Mineralium Deposita 34, 71–81.

Buttermann, W.C., Foster, W.R., 1967. Zircon stability and the ZrO_2–SiO_2 phase diagram. American Mineralogist 52, 880–885.

Cayzer, N.J., Odake, S., Harte, B., Kagi, H., 2008. Plastic deformation of lower mantle diamonds by inclusion phase transformations. European Journal of Mineralogy 20 (3), 333–339.

Cesbron, F., Blanc, P., Ohnenstetter, D., Rémond, G., 1995. Cathodoluminescence of rare earth doped zircons: I. Their possible use as reference materials. Scanning Microscopy Supplement 9, 35–56.

Cherniak, D.J., Hanchar, J.M., E.B., W., 1997. Rare-earth diffusion in zircon. Chemical Geology 134, 289–301.

Cherniak, D.J., Watson, E.B., 2003. Diffusion in zircon. In: Hanchar, J.M., Hoskin, P.W.O. (Eds.), Reviews in Mineralogy and Geochemistry: Zircon. Reviews in Mineralogy and Geochemistry, vol. 53. Mineralogical Society of America, pp. 113–143.

Chupin, S.V., Chupin, V.P., Barton, J.M., Barton, E.S., 1998. Archean melt inclusions in zircon from quartzite and granitic orthogneiss from South Africa; magma compositions and probable sources of protoliths. European Journal of Mineralogy 10 (6), 1241–1251.

Cordier, P., Doukhan, J.C., 1989. Water solubility in quartz and its influence on ductility. European Journal of Mineralogy 1 (2), 221–237.

Corfu, F., Hanchar, J.M., Hoskin, P.W.O., Kinny, P., 2003. Atlas of zircon textures. In: Hanchar, J.M., Hoskin, P.W.O. (Eds.), Reviews in Mineralogy and Geochemistry: Zircon, vol. 53. Mineralogical Society of America, pp. 469–500.

Cottrell, A.H., 1958. Transactions Metallurgy Society AIME 212, 192–203.

Danyushevsky, L.V., McNeill, A.W., Sobolev, A.V., 2002. Experimental and petrological studies of melt inclusions in phenocrysts from mantle-derived magmas: an overview of techniques, advantages and complications. Chemical Geology 183 (1–4), 5–24.

Delle Piane, C., Wilson, C.J.L., Burlini, L., 2009. Dilatant plasticity in high-strain experiments on calcite-muscovite aggregates. Journal of Structural Geology 31 (10), 1084–1099.

Dyson, B.F., 1983. Continuous cavity nucleation and creep fracture. Scripta Metallurgica 17 (1), 31–37.

Eshelby, J.D., 1959. The elastic field outside an ellipsoidal inclusion, and related problems. Proceedings of the Royal Society of London A252, 561–569.

Fusseis, F., Regenauer-Lieb, K., Liu, J., Hough, R.M., De Carlo, F., 2009. Creep cavitation can establish a dynamic granular fluid pump in ductile shear zones. Nature 459 (7249), 974–977.

Gaft, M., Panczer, G., Reisfeld, R., Shinno, I., 2000. Laser-induced luminescence of rare-earth elements in natural zircon. Journal of Alloys and Compounds 300–301, 267–274.

Geisler, T., Ulonska, M., Schleicher, H., Pidgeon, R.T., van Bronswijk, W., 2001. Leaching and differential recrystallization of metamict zircon under experimental hydrothermal conditions. Contributions to Mineralogy and Petrology 141 (1), 53–65.

Geisler, T., Zhang, M., Salje, E.K.H., 2003. Recrystallization of almost fully amorphous zircon under hydrothermal conditions: an infrared spectroscopic study. Journal of Nuclear Materials 320 (3), 280–291.

Gerald, J.D.F., Boland, J.N., McLaren, A.C., Ord, A., Hobbs, B.E., 1991. Microstructures in water-weakened single crystals of quartz. Journal of Geophysical Research 96 (B2), 2139–2155.

Glass, B.P., Liu, S., Glass, B.P., Fries, M., 2001. Discovery of high-pressure ZrSiO4 polymorph in naturally occurring shock-metamorphosed zircons: micro-Raman spectroscopic study of fine-grained, shock-metamorphosed rock fragments from the Australasian microtektite layer. Geology 29 (4), 371–373.

Green II, H.W., Gueguen, Y., 1983. Deformation of peridotite in the mantle and extraction by kimberlite: a case history documented by fluid and solid precipitates in olivine. Tectonophysics 92 (1–3), 71–92.

Hazen, R.M., Finger, L.W., 1979. Crystal structure and compressibility of zircon at high pressure. American Mineralogist 64, 196–201.

Healy, D., 2009. Elastic field in 3D due to a spheroidal inclusion–MATLAB(TM) code for Eshelby's solution. Computers & Geosciences 35 (10), 2170–2173.

Hirth, G., Tullis, J., 1992. Dislocation creep regimes in quartz aggregates. Journal of Structural Geology 14 (2), 145–159.

Hopkins, M.D., Harrison, T.M., Manning, C.E., 2010. Constraints on Hadean geodynamics from mineral inclusions in >4 Ga zircons. Earth and Planetary Science Letters 298 (3–4), 367–376.

Kaczmarek, M.A., Reddy, S.M., Timms, N.E., 2011. Evolution of zircon deformation mechanisms in a shear zone (Lanzo massif, Western-Alps). Lithos 127 (3–4), 414–426.

Kassner, M.E., Hayes, T.A., 2003. Creep cavitation in metals. International Journal of Plasticity 19 (10), 1715–1748.

Katayama, I., Maruyama, S., 2009. Inclusion study in zircon from ultrahigh-pressure metamorphic rocks in the Kokchetav massif: an excellent tracer of metamorphic history. Journal of the Geological Society 166 (4), 783–796.

Katayama, I., Ohta, M., Ogasawara, Y., 2002. Mineral inclusions in zircon from diamond-bearing marble in the Kokchetav massif, northern Kazakhstan. European Journal of Mineralogy 14 (6), 1103–1108.

Leroux, H., Reimold, W.U., Koeberl, C., Hornemann, U., Doukhan, J.C., 1999. Experimental shock deformation in zircon: a transmission electron microscopic study. Earth and Planetary Science Letters 169 (3–4), 291–301.

Li, Z., 1994. The silicate melt inclusions of igneous rocks. In: De Vivo, B., Frezzotti, M.L. (Eds.), Fluid Inclusions in Minerals: Methods and Applications. Virginia Tech, Blacksburgh, Virginia, pp. 73–94.

Liu, F., Xu, Z., Xue, H., 2004. Tracing the protolith, UHP metamorphism, and exhumation ages of orthogneiss from the SW Sulu terrane (eastern China): SHRIMP U-Pb dating of mineral inclusion-bearing zircons. Lithos 78 (1–4), 411–429.

Lloyd, G.E., 1987. Atomic number and crystallographic contrast images with the SEM: a review of backscattered electron techniques. Mineralogical Magazine 51, 3–19.

MacRae, C.M., Wilson, N.C., Johnson, S.A., Phillips, P.L., Otsuki, M., 2005. Hyperspectral mapping - combining cathodoluminescence and X-ray collection in an electron microprobe. Microscopy Research and Technique 67 (5), 271–277.

Mancktelow, N.S., Grujic, D., Johnson, E.L., 1998. An SEM study of porosity and grain boundary microstructure in quartz mylonites, simplon fault zone, central alps. Contributions to Mineralogy and Petrology 131 (1), 71–85.

Massonne, H.-J., Nasdala, L., 2003. Characterization of an early metamorphic stage through inclusions in zircon of a diamondiferous quartzofeldspathic rock from the Erzgebirge, Germany. American Mineralogist 88 (5–6), 883–889.

Menneken, M., Nemchin, A.A., Geisler, T., Pidgeon, R.T., Wilde, S.A., 2007. Hadean diamonds in zircon from Jack Hills, Western Australia. Nature 448 (7156), 917–920.

Moser, D.E., Davis, W.J., Reddy, S.M., Flemming, R.L., Hart, R.J., 2009. Zircon U-Pb strain chronometry reveals deep impact-triggered flow. Earth and Planetary Science Letters 277 (1–2), 73–79.

Nasdala, L., Hofmeister, W., Harris, J.W., Glinnemann, J., 2005. Growth zoning and strain patterns inside diamond crystals as revealed by Raman maps. American Mineralogist 90 (4), 745–748.

Nasdala, L., Kronz, A., Wirth, R., Blanc, P., Kennedy, A.K., Seydoux-Guillaume, A.M., Lengauer, C.L., Hanchar, J.M., 2002. Annealing radiation damage and the recovery of cathodoluminescence. Chemical Geology 191 (1–3), 121–140.

Nasdala, L., Zhang, M., Kempe, U., Panczer, G., Gaft, M., Andrut, M., Plotze, M., 2003. Spectroscopic methods applied to zircon. In: Hanchar, J.M., Hoskin, P.W.O. (Eds.), Reviews in Mineralogy and Geochemistry: Zircon. Reviews in Mineralogy and Geochemistry, vol. 53. Mineralogical Society of America, pp. 427–467.

Nemchin, A., Timms, N.E., Pidgeon, R., Geisler, T., Reddy, S.M., Meyer, C., 2009. Timing of crystallization of the lunar magma ocean constrained by the oldest zircon. Nature Geoscience 2, 133–136.

Nemchin, A.A., Whitehouse, M.J., Menneken, M., Geisler, T., Pidgeon, R.T., Wilde, S.A., 2008. A light carbon reservoir recorded in zircon-hosted diamond from the Jack Hills. Nature 454 (7200), 92–95.

Prior, D.J., Boyle, A.P., Brenker, F., Cheadle, M.C., Day, A., Lopez, G., Peruzzo, L., Potts, G.J., Reddy, S., Spiess, R., Timms, N.E., Trimby, P., Wheeler, J., Zetterström, L., 1999. The application of electron backscatter diffraction and orientation contrast imaging in the SEM to textural problems in rocks. American Mineralogist 84 (11–12), 1741–1759.

Prior, D.J., Wheeler, J., Peruzzo, L., Spiess, R., Storey, C., 2002. Some garnet microstructures: an illustration of the potential of orientation maps and misorientation analysis in microstructural studies. Journal of Structural Geology 24, 999–1011.

Qin, Z., 1992. Disequilibrium partial melting model and its implication for trace elements fractionations during mantle melting. Earth and Planetary Science Letters 112, 75–90.

Raj, R., Ashby, M.F., 1975. Intergranular fracture at elevated temperature. Acta Metallurgica 23 (6), 653–666.

Reddy, S.M., Timms, N.E., Eglington, B.M., 2008. Electron backscatter diffraction analysis of zircon: a systematic assessment of match unit characteristics and pattern indexing optimization. American Mineralogist 93, 187–197.

Reddy, S.M., Timms, N.E., Hamilton, P.J., Smyth, H.R., 2009. Deformation-related microstructures in magmatic zircon and implications for diffusion. Contributions to Mineralogy and Petrology 157 (2), 231–244.

Reddy, S.M., Timms, N.E., Pantleon, W., Trimby, P., 2007. Quantitative characterization of plastic deformation of zircon and geological implications. Contributions to Mineralogy and Petrology 153, 625–645.

Reddy, S.M., Timms, N.E., Trimby, P., Kinny, P.D., Buchan, C., Blake, K., 2006. Crystal-plastic deformation of zircon: a defect in the assumption of chemical robustness. Geology 34, 257–260.

Remond, G., Cesbron, F., Chapoulie, R., Ohnenstetter, D., Roquescarmes, C., Schvoerer, M., 1992. Cathodoluminescence applied to the microcharacterization of mineral materials - a present status in experimentation and interpretation. Scanning Microscopy 6 (1), 23–68.

Rybacki, E., Wirth, R., Dresen, G., 2008. High-strain creep of feldspar rocks: implications for cavitation and ductile failure in the lower crust. Geophysical Research Letters 35, L04304.

Smyth, H.R., Hamilton, P.J., Hall, R., Kinny, P.D., 2007. The deep crust beneath island arcs: inherited zircons reveal a Gondwana continental fragment beneath East Java, Indonesia. Earth and Planetary Science Letters 258 (1–2), 269–282.

Stroh, A.N., 1957. A theory of the fracture of metals. Advances in Physics 6, 418–465.

Stünitz, H., Fitz Gerald, J.D., Tullis, J., 2003. Dislocation generation, slip systems, and dynamic recrystallization in experimentally deformed plagioclase single crystals. Tectonophysics 372 (3–4), 215–233.

Thomas, J.B., Bodnar, R.J., Shimizu, N., Chesner, C.A., 2003. Melt inclusions in zircon. Reviews in Mineralogy and Geochemistry 53 (1), 63–87.

Thomas, J.B., Bodnar, R.J., Shimizu, N., Sinha, A.K., 2002. Determination of zircon/melt trace element partition coefficients from SIMS analysis of melt inclusions in zircon. Geochimica et Cosmochimica Acta 66 (16), 2887–2901.

Timms, N., Kinny, P., Reddy, S., 2006. Enhanced diffusion of uranium and thorium linked to crystal plasticity in zircon. Geochemical Transactions 7 (1), 10.

Timms, N.E., Kinny, P.D., Reddy, S.M., Evans, K., Clark, C., Healy, D., 2011. Relationship among titanium, rare earth elements, U-Pb ages and deformation microstructures in zircon: implications for Ti-in-zircon thermometry. Chemical Geology 280 (1–2), 33–46.

Timms, N.E., Li, J., Reddy, S.M., 2009. Quantitative microstructural characterization of natrojarosite scale formed during high-pressure acid leaching of lateritic nickel ore. American Mineralogist 94 (8–9), 1111–1119.

Timms, N.E., Reddy, S.M., 2009. Response of cathodoluminescence to crystal-plastic deformation in zircon. Chemical Geology 261, 11–23.

Timms, N. E., Reddy, S. M., Healy, D., Nemchin, A. A., Grange, M. L., Pidgeon, R. T. & Hart, R. D. in press. Resolution of impact-related microstructures in lunar zircon: a shock-deformation mechanism map. Meteoritics and Planetary Science. doi:10.1111/j.1945-5100.2011.01316.x.

Trepmann, C.A., Stöckhert, B., 2003. Quartz microstructures developed during nonsteady state plastic flow at rapidly decaying stress and strain rate. Journal of Structural Geology 25 (12), 2035–2051.

Vernooij, M.G.C., Kunze, K., den Brok, B., 2006. 'Brittle' shear zones in experimentally deformed quartz single crystals. Journal of Structural Geology 28 (7), 1292–1306.

Weertman, J., 1986. Zener-Stroh crack, Zener-Hollomon parameter, and other topics. Journal of Applied Physics 60 (6), 1877–1887.

Westwood, C., Pan, J., Crocombe, A.D., 2004. Nucleation, growth and coalescence of multiple cavities at a grain-boundary. European Journal of Mechanics - A/Solids 23 (4), 579–597.

Wittmann, A., Kenkmann, T., Schmitt, R.T., Stöffler, D., 2006. Shock-metamorphosed zircon in terrestrial impact craters. Meteorics & Planetary Science 41 (3), 433–454.